LETTER

doi:10.1038/nature24290

The X-ray counterpart to the gravitational-wave event GW170817

E. Troja[1,2], L. Piro[3], H. van Eerten[4], R. T. Wollaeger[5], M. Im[6], O. D. Fox[7], N. R. Butler[8], S. B. Cenko[2,9], T. Sakamoto[10], C. L. Fryer[5], R. Ricci[11], A. Lien[2,12], R. E. Ryan Jr[7], O. Korobkin[5], S.-K. Lee[6], J. M. Burgess[13], W. H. Lee[14], A. M. Watson[14], C. Choi[6], S. Covino[15], P. D'Avanzo[15], C. J. Fontes[5], J. Becerra González[16,17], H. G. Khandrika[7], J. Kim[6], S.-L. Kim[18], C.-U. Lee[18], H. M. Lee[19], A. Kutyrev[1,2], G. Lim[6], R. Sánchez-Ramírez[3], S. Veilleux[1,9], M. H. Wieringa[20] & Y. Yoon[6]

A long-standing paradigm in astrophysics is that collisions—or mergers—of two neutron stars form highly relativistic and collimated outflows (jets) that power γ-ray bursts of short (less than two seconds) duration[1–3]. The observational support for this model, however, is only indirect[4,5]. A hitherto outstanding prediction is that gravitational-wave events from such mergers should be associated with γ-ray bursts, and that a majority of these bursts should be seen off-axis, that is, they should point away from Earth[6,7]. Here we report the discovery observations of the X-ray counterpart associated with the gravitational-wave event GW170817. Although the electromagnetic counterpart at optical and infrared frequencies is dominated by the radioactive glow (known as a 'kilonova') from freshly synthesized rapid neutron capture (r-process) material in the merger ejecta[8–10], observations at X-ray and, later, radio frequencies are consistent with a short γ-ray burst viewed off-axis[7,11]. Our detection of X-ray emission at a location coincident with the kilonova transient provides the missing observational link between short γ-ray bursts and gravitational waves from neutron-star mergers, and gives independent confirmation of the collimated nature of the γ-ray-burst emission.

On 17 August 2017 at 12:41:04 universal time (UT; hereafter T_0), the Advanced Laser Interferometer Gravitational-Wave Observatory (LIGO) detected a gravitational-wave transient from the merger of two neutron stars at a distance[12] of 40 ± 8 Mpc. Approximately two seconds later, a weak γ-ray burst (GRB) of short duration (<2 s) was observed by the Fermi Gamma-ray Space Telescope[13] and INTEGRAL[14]. The low luminosity of this γ-ray transient was unusual compared to the population of short GRBs at cosmological distances[15], and its physical connection with the gravitational-wave event remained unclear.

A vigorous observing campaign targeted the localization region of the gravitational-wave transient, and rapidly identified a source of bright optical, infrared and ultraviolet emission in the early-type galaxy NGC 4993[16,17]. This source was designated 'SSS17a' by the Swope team[16], but here we use the official IAU designation, AT 2017gfo.

AT 2017gfo was initially not visible at radio and X-ray wavelengths. However, on 26 August 2017, we observed the field with the Chandra X-ray Observatory and detected X-ray emission at the position of AT 2017gfo (Fig. 1). The observed X-ray flux (see Methods) implies an isotropic luminosity of 9×10^{38} erg s^{-1} if located in NGC 4993 at a distance of about 40 Mpc. Further Chandra observations, performed between 1 and 2 September 2017, confirmed the presence

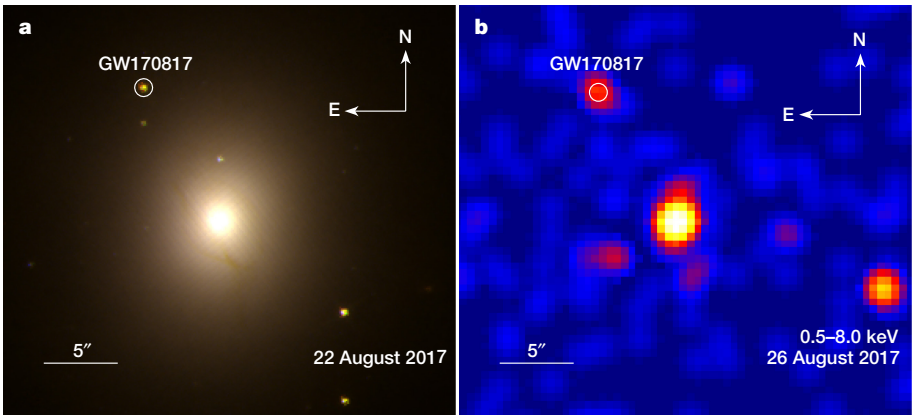

Figure 1 | Optical/infrared and X-ray images of the counterpart of GW170817. a, Hubble Space Telescope observations show a bright and red transient in the early-type galaxy NGC 4993, at a projected physical offset of about 2 kpc from its nucleus. A similar small offset is observed in less than a quarter of short GRBs[5]. Dust lanes are visible in the inner regions, suggestive of a past merger activity (see Methods). **b**, Chandra observations revealed a faint X-ray source at the position of the optical/infrared transient. X-ray emission from the galaxy nucleus is also visible.

[1]Department of Astronomy, University of Maryland, College Park, Maryland 20742-4111, USA. [2]Astrophysics Science Division, NASA Goddard Space Flight Center, 8800 Greenbelt Road, Greenbelt, Maryland 20771, USA. [3]INAF, Istituto di Astrofisica e Planetologia Spaziali, via Fosso del Cavaliere 100, 00133 Rome, Italy. [4]Department of Physics, University of Bath, Claverton Down, Bath BA2 7AY, UK. [5]Center for Theoretical Astrophysics, Los Alamos National Laboratory, Los Alamos, New Mexico 87545, USA. [6]Center for the Exploration for the Origin of the Universe, Astronomy Program, Department of Physics and Astronomy, Seoul National University, 1 Gwanak-ro, Gwanak-gu, Seoul 08826, South Korea. [7]Space Telescope Science Institute, Baltimore, Maryland 21218, USA. [8]School of Earth and Space Exploration, Arizona State University, Tempe, Arizona 85287, USA. [9]Joint Space-Science Institute, University of Maryland, College Park, Maryland 20742, USA. [10]Department of Physics and Mathematics, Aoyama Gakuin University, 5-10-1 Fuchinobe, Chuo-ku, Sagamihara-shi Kanagawa 252-5258, Japan. [11]INAF-Istituto di Radioastronomia, Via Gobetti 101, I-40129, Italy. [12]Department of Physics, University of Maryland, Baltimore County, 1000 Hilltop Circle, Baltimore, Maryland 21250, USA. [13]Max-Planck-Institut für extraterrestrische Physik, Giessenbachstrasse, D-85748 Garching, Germany. [14]Instituto de Astronomía, Universidad Nacional Autónoma de México, Apartado Postal 70-264, 04510 Ciudad de México, México. [15]INAF/Brera Astronomical Observatory, via Bianchi 46, Merate, Italy. [16]Instituto de Astrofísica de Canarias, E-38200 La Laguna, Spain. [17]Universidad de La Laguna, Departimento of Astrofísica, E-38206 La Laguna, Spain. [18]Korea Astronomy and Space Science Institute, 776 Daedeokdae-ro, Yuseong-gu, Daejeon 34055, South Korea. [19]Astronomy Program, Department of Physics and Astronomy, Seoul National University, 1 Gwanak-ro, Gwanak-gu, Seoul 08826, South Korea. [20]CSIRO Astronomy and Space Science, PO Box 76, Epping, New South Wales 1710, Australia.

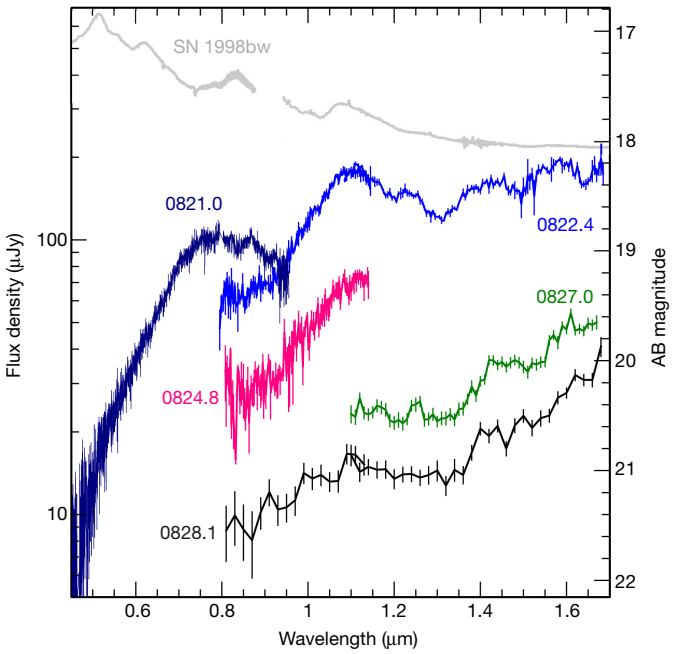

Figure 2 | Optical and infrared spectra of the kilonova associated with GW170817. The optical spectrum, acquired on 21 August 2017 ($T_0 + 3.5$ d) with the Gemini South 8-m telescope, is dominated by a featureless continuum with a rapid turnover above a wavelength of about 0.75 μm. At later times, this feature is no longer visible. Near-infrared spectra, taken with the Hubble Space Telescope between 22 and 28 August 2017, show prominent broad ($\Delta\lambda/\lambda \approx 0.1$) features and a slow evolution towards redder colours. These spectral features are consistent with the ejection of high-velocity, neutron-rich material during a neutron-star merger. The colour-coded numbers indicate the epoch of each spectrum. A spectrum of the broad-lined type Ic supernova SN 1998bw (8 days post-maximum; arbitrarily rescaled) is shown for comparison. Error bars are 1σ.

of continued X-ray activity, and hinted at a slight increase in luminosity to $L_{\rm X,iso} \approx 1.1 \times 10^{39}$ erg s^{-1}. At a similar epoch the onset of radio emission was also detected[18].

The evolution of AT 2017gfo across the electromagnetic spectrum shows multiple components dominating the observed emission. Simple modelling of the optical–infrared photometry as a blackbody in linear expansion suggests mildly relativistic ($\geq 0.2c$, where c is the speed of light in vacuum) velocities and cool ($<$10,000 K) temperatures. We find a hot blue component, mainly contributing at optical wavelengths, and a colder infrared component, which progressively becomes redder (Extended Data Fig. 1). The low peak luminosity ($M_{\rm V} \approx -16$) and featureless optical spectrum (Fig. 2) disfavour a supernova explosion (see Methods), while the broad ($\Delta\lambda/\lambda \approx 0.1$) features in the infrared spectra are consistent with expectations for rapidly expanding dynamical ejecta[9,10], rich in lanthanides and actinides formed via rapid neutron capture nucleosynthesis (the r-process). The overall properties of the host galaxy, such as its stellar mass, evolved stellar population and low star formation (see Methods), are consistent with the typical environment of short GRBs and in line with the predictions for compact binary mergers[5]. When combined, these data point to a kilonova emission, consisting of the superposition of radioactive-powered emission from both neutron-rich dynamical ejecta expanding with velocity $v \approx 0.2c$ and a slower, sub-relativistic wind with a higher electron fraction[19]. The former component radiates most of its energy in the infrared, while the latter dominates the optical and ultraviolet spectrum. The optical/infrared data set therefore provides convincing evidence that AT 2017gfo was a kilonova produced by the merger of two compact objects, at a time and location consistent with GW170817.

Our Chandra observations at $T_0 + 9$ d revealed the onset of a new emission component at X-ray energies. Although the basic model for kilonovae does not predict detectable X-ray emission, previous candidate kilonovae were all associated with an X-ray brightening. This led to the suggestion that the power source of the infrared transient may be thermal re-emission of the X-ray photons rather than radioactive heat[20]. However, in these past cases[20–22], the X-ray luminosity was comparable to or higher than the optical/infrared component, whereas in our case the infrared component is clearly dominant and 20 times brighter than the faint X-ray emission. These different luminosities and temporal behaviours suggest that the X-ray emission is instead decoupled from the kilonova.

The interaction of the fast-moving ejecta with the circumstellar material may produce detectable emission[23]. An ambient density $n > 10^3$ cm^{-3} would be required to explain the observed onset at about $T_0 + 9$ d, but neither the optical nor the X-ray spectra show any evidence for absorption from this dense intervening medium. After a binary neutron-star merger, X-rays could be produced by a rapidly rotating and highly magnetized neutron star. However, none of the current models[21,24] can reproduce persistent emission over the observed timescales of around two weeks. Fallback accretion[25] of the merger ejecta could account for such long-lived faint X-ray emission; however, the predicted thermal spectrum should not be visible at radio frequencies. Instead, a more likely explanation, also supported by the detection of a radio counterpart, is that the observed X-rays are synchrotron afterglow radiation from the short GRB 170817A. By assuming that radio and X-ray emission belong to the same synchrotron regime, we derive a spectral slope of $\beta \approx 0.64$, consistent with the index measured from the X-ray spectrum (see Methods) and with typical values of GRB afterglow spectra[15]. Therefore, our detection of X-ray emission at the same position as AT 2017gfo (see Methods) shows that the short GRB and the optical/infrared transient are co-located, establishing a direct link between GRB 170817A, its kilonova and GW170817.

In the standard GRB model[26], the broadband afterglow emission is produced by the interaction of the jet with the surrounding medium. For an observer on the jet axis, the afterglow appears as a luminous ($L_{\rm X,iso} > 10^{44}$ erg s^{-1}) fading transient visible across the electromagnetic spectrum from the first few minutes after the burst. This is not consistent with our observations. If the observer is instead viewing beyond the opening angle $\theta_{\rm j}$ of the jetted outflow, relativistic beaming will weaken the emission in the observer's direction by orders of magnitude. The afterglow only becomes apparent once the jet has spread and decelerated sufficiently that the beaming cone of the emission includes the observer[7,10]. Therefore, an off-axis observer sees that the onset of the afterglow is delayed by several days or weeks. In our case, the slow rise of the X-ray emission suggests that our observations took place near the peak time $t_{\rm peak}$ of the off-axis afterglow light curve, predicted to follow $t_{\rm peak} \propto E_{\rm k,iso}^{1/3} n^{-1/3} (\theta_{\rm v} - \theta_{\rm j})^{2.5}$, where $E_{\rm k,iso}$ is the isotropic-equivalent blastwave energy. The off-axis angle $\Delta\theta$ is therefore constrained as $\Delta\theta = \theta_{\rm v} - \theta_{\rm j} \approx 13^\circ \times t_{\rm peak}^{2/5} \times E_{\rm k,iso}^{-2/15} \times n^{2/15}$, where $t_{\rm peak}$ is given in units of 15 d, $E_{\rm k,iso}$ is in units of 10^{50} erg and n is in units of 10^{-3} cm^{-3}.

In Fig. 3a we show that our dataset can be reproduced by a standard short GRB afterglow[15] with the only difference being the viewing angle: on-axis ($\theta_{\rm v} \ll \theta_{\rm j}$) in the commonly observed scenario, and off-axis ($\theta_{\rm v} > \theta_{\rm j}$) in our case. The synthetic light curves were produced from two-dimensional jet simulations[27], but the key features of these curves are general to spreading ejecta seen off-axis (see Methods for further details; also Extended Data Fig. 2). Our observations therefore independently confirm the collimated nature of GRB outflows[28].

Interestingly, all three observed electromagnetic counterparts (GRB, kilonova and afterglow) separately point at a substantial offset of the binary orbital plane axis relative to the observer, independent of any constraint arising directly from the gravitational-wave event. The initial γ-ray emission is unusually weak, being orders of magnitude less luminous than typical short GRBs. This suggests a large angle between the jet and the observer. The standard top-hat profile that is usually adopted to describe GRB jets cannot easily account for the observed

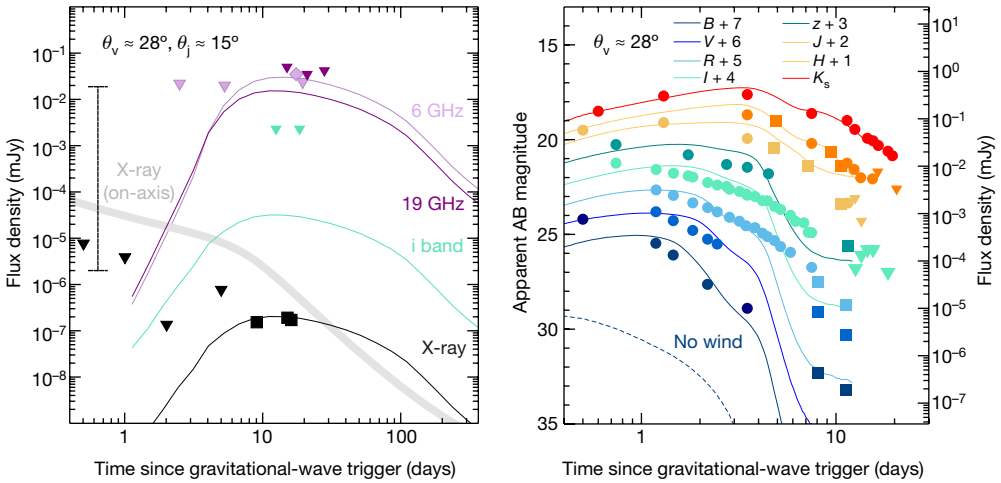

Figure 3 | Multi-wavelength light curves for the counterpart of GW170817. a, Temporal evolution of the X-ray and radio counterparts of GW170817 compared to the model predictions (thin solid lines) for a short GRB afterglow viewed at an angle $\theta_v \approx 28°$. The thick grey line shows the X-ray light curve of the same afterglow as seen on-axis, falling in the typical range[15] of short GRBs (vertical dashed line). Upper limits are 3σ. **b**, Temporal evolution of the optical and infrared transient AT 2017gfo compared with the theoretical predictions (solid lines) for a kilonova seen off-axis with viewing angle $\theta_v \approx 28°$. For comparison with the ground-based photometry, Hubble Space Telescope measurements (squares) were converted to standard filters. Our model includes the contribution from a massive, high-speed wind along the polar axis ($M_w \approx 0.015 M_\odot$, $v \approx 0.08c$) and from the dynamical ejecta ($M_{ej} \approx 0.002 M_\odot$, $v \approx 0.2c$). The presence of a wind is required to explain the bright and long-lived optical emission, which is not expected otherwise (see dashed line).

properties of GRB 170817A (see Methods). Instead, a structured jet profile, where the outflow energetics and Lorentz factor vary with the angle from the jet axis, can explain both the GRB and afterglow properties (Extended Data Fig. 3). Alternatively, the low-luminosity γ-ray transient may not trace the prompt GRB emission, but come from a broader collimated, mildly relativistic cocoon[29].

Another independent constraint on the off-axis geometry comes from the spectral and temporal evolution of the kilonova light curves (Fig. 3b). The luminous and long-lived optical emission implies that the observer intercepts a substantial contribution from the wind component along the polar axis, which would be shielded by the lanthanide-rich ejecta for an edge-on observer along the equatorial plane (Fig. 4). A comparison between the kilonova models[30] and our optical-infrared photometry favours an off-axis orientation, in which the wind is partially obscured by the dynamical ejecta, with an estimated inclination angle anywhere between 20° and 60° (Extended Data Fig. 4), depending on the detailed configuration of the dynamical ejecta. Taking into account the uncertainties in the model, such as the morphologies of the ejecta and the possible different types of wind, this is in good agreement with the orientation inferred from afterglow modelling. The geometry of the binary merger GW170817 (Fig. 4), here primarily constrained through electromagnetic observations, could be further refined through a joint analysis with the gravitational-wave signal.

The discovery of GW170817 and its X-ray counterpart shows that the second generation of gravitational-wave interferometers will enable us to uncover a new population of weak and probably off-axis GRBs associated with gravitational-wave sources, thus providing an unprecedented opportunity to investigate the properties of these cosmic explosions and their progenitors. This paves the way for multi-messenger (that is, electromagnetic and gravitational-wave radiation) modelling of the different aspects of these events, which may potentially help to break the degeneracies that exist in the models of neutron-star mergers when considered separately.

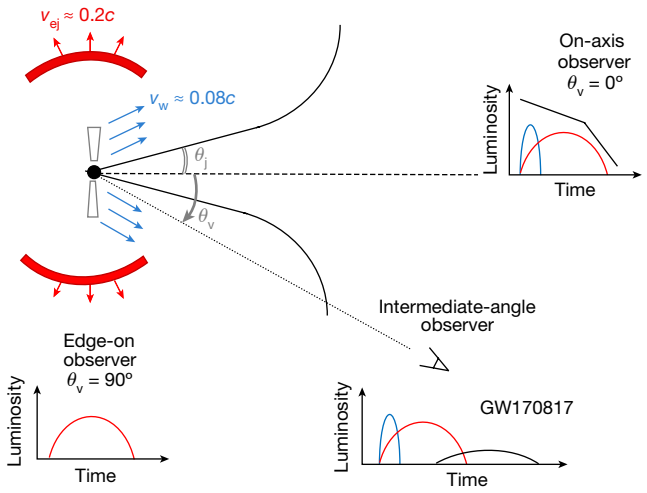

Figure 4 | Schematic diagram for the geometry of GW170817. Following the neutron-star merger, a small amount of fast-moving neutron-rich ejecta (red shells) emits an isotropic kilonova peaking in the infrared. A larger mass neutron-free wind along the polar axis (blue arrows) produces kilonova emission peaking at optical wavelengths. This emission, although isotropic, is not visible to edge-on observers because it is only visible within a range of angles and otherwise shielded by the high-opacity ejecta. A collimated jet (black solid cone) emits synchrotron radiation visible at radio, X-ray and optical wavelengths. This afterglow emission outshines all other components if the jet is seen on-axis. However, to an off-axis observer, it appears as a low-luminosity component delayed by several days or weeks.

Online Content Methods, along with any additional Extended Data display items and Source Data, are available in the online version of the paper; references unique to these sections appear only in the online paper.

Received 12 September; accepted 21 September 2017.
Published online 16 October 2017.

1. Eichler, D., Livio, M., Piran, T. & Schramm, D. N. Nucleosynthesis, neutrino bursts and gamma-rays from coalescing neutron stars. *Nature* **340,** 126–128 (1989).
2. Kouveliotou, C. *et al.* Identification of two classes of gamma-ray bursts. *Astrophys. J.* **413,** L101–L104 (1993).
3. Rezzolla, L. *et al.* The missing link: merging neutron stars naturally produce jet-like structures and can power short gamma-ray bursts. *Astrophys. J.* **732,** L6 (2011).
4. Gehrels, N. *et al.* A short γ-ray burst apparently associated with an elliptical galaxy at redshift $z = 0.225$. *Nature* **437,** 851–854 (2005).

5. Berger, E. Short-duration gamma-ray bursts. *Annu. Rev. Astron. Astrophys.* **52,** 43–105 (2014).
6. Schutz, B. F. Networks of gravitational wave detectors and three figures of merit. *Class. Quantum Gravity* **28,** 125023 (2011).
7. Rhoads, J. E. How to tell a jet from a balloon: a proposed test for beaming in gamma-ray bursts. *Astrophys. J.* **487,** L1–L4 (1997).
8. Li, L.-X. & Paczynski, B. Transient events from neutron star mergers. *Astrophys. J.* **507,** L59–L62 (1998).
9. Metzger, B. D. *et al.* Electromagnetic counterparts of compact object mergers powered by the radioactive decay of r-process nuclei. *Mon. Not. R. Astron. Soc.* **406,** 2650–2662 (2010).
10. Piran, T., Nakar, E. & Rosswog, S. The electromagnetic signals of compact binary mergers. *Mon. Not. R. Astron. Soc.* **430,** 2121–2136 (2013).
11. van Eerten, H. J., Zhang, W. & MacFadyen, A. I. Off-axis gamma-ray burst afterglow modeling based on a two-dimensional axisymmetric hydrodynamics simulation. *Astrophys. J.* **722,** 235–247 (2010).
12. LIGO Scientific Collaboration and Virgo Collaboration. GW170817: observation of gravitational waves from a binary neutron star inspiral. *Phys. Rev. Lett.* https://doi.org/10.1103/PhysRevLett.119.161101 (2017).
13. Goldstein, A. *et al.* An ordinary short gamma-ray burst with extraordinary implications: Fermi-GBM detection of GRB 170817A. *Astrophys. J.* **848,** https://doi.org/10.3847/2041-8213/aa8f41 (2017).
14. Savchenko, V. *et al.* INTEGRAL detection of the first prompt gamma-ray signal coincident with the gravitational wave event GW170817. *Astrophys. J.* **848,** https://doi.org/10.3847/2041-8213/aa8f94 (2017).
15. D'Avanzo, P. *et al.* A complete sample of bright Swift short gamma-ray bursts. *Mon. Not. R. Astron. Soc.* **442,** 2342–2356 (2014).
16. Coulter, D. A. *et al.* Swope supernova survey 2017a (SSS17a), the optical counterpart to a gravitational wave source. *Science* http://doi.org/10.1126/science.aap9811 (2017).
17. Evans, P. A. *et al.* Swift and NuSTAR observations of GW170817: detection of a blue kilonova. *Science* http://doi.org/10.1126/science.aap9580 (2017).
18. Hallinan, G. *et al.* A radio counterpart to a neutron star merger. *Science* http://doi.org/10.1126/science.aap9855 (2017).
19. Grossman, D., Korobkin, O., Rosswog, S. & Piran, T. The long-term evolution of neutron star merger remnants—II. Radioactively powered transients. *Mon. Not. R. Astron. Soc.* **439,** 757–770 (2014).
20. Kisaka, S., Ioka, K. & Nakar, E. X-ray-powered macronovae. *Astrophys. J.* **818,** 104 (2016).
21. Gao, H., Ding, X., Wu, X.-F., Dai, Z.-G. & Zhang, B. GRB 080503 late afterglow re-brightening: signature of a magnetar-powered merger-nova. *Astrophys. J.* **807,** 163 (2015).
22. Jin, Z.-P. *et al.* The macronova in GRB 050709 and the GRB-macronova connection. *Nat. Commun.* **7,** 12898 (2016).
23. Nakar, E. & Piran, T. Detectable radio flares following gravitational waves from mergers of binary neutron stars. *Nature* **478,** 82–84 (2011).
24. Zhang, B. & Meszaros, P. Gamma-ray burst afterglow with continuous energy injection: signature of a highly magnetized millisecond pulsar. *Astrophys. J.* **552,** L35–L38 (2001).
25. Rossi, E. M. & Begelman, M. C. Delayed X-ray emission from fallback in compact-object mergers. *Mon. Not. R. Astron. Soc.* **392,** 1451–1455 (2009).
26. Piran, T. Gamma-ray bursts and the fireball model. *Phys. Rep.* **314,** 575–667 (1999).
27. Van Eerten, H., van der Horst, A. & MacFadyen, A. Gamma-ray burst afterglow broadband fitting based directly on hydrodynamics simulations. *Astrophys. J.* **749,** 44 (2012).
28. Troja, E. *et al.* An achromatic break in the afterglow of the short GRB 140903A: evidence for a narrow jet. *Astrophys. J.* **827,** 102 (2016).
29. Lazzati, D. *et al.* Off-axis prompt X-ray transients from the cocoon of short gamma-ray bursts. Preprint at https://arxiv.org/abs/1709.01468 (2017).
30. Wollaeger, R. T. *et al.* Impact of ejecta morphology and composition on the electromagnetic signatures of neutron star mergers. Preprint at https://arxiv.org/abs/1705.07084 (2017).

Acknowledgements We acknowledge the advice and contribution of N. Gehrels, who was co-investigator of our Chandra and Hubble Space Telescope observing programs. We thank B. Wilkes and the Chandra X-ray Center staff, N. Reid and the Space Telescope Science Institute (STScI) staff, J. Stevens and the CSIRO staff, L. Ferrarese and the Gemini support staff, in particular R. Salinas, M. Andersen, H. Kim, P. Candia and K. Silva. E. Troja thanks Bianca A. Vekstein, A. Bersich and F. Troja for help during the preparation of this manuscript. We thank V. Bajaj (STScI) and S. Hernandez for their assistance with data reduction. Work at LANL was done under the auspices of the National Nuclear Security Administration of the US Department of Energy at Los Alamos National Laboratory (LANL) under contract number DE-AC52-06NA25396. All LANL calculations were performed on LANL Institutional Computing resources. This research used resources provided by the LANL Institutional Computing Program, which is supported by the US Department of Energy National Nuclear Security Administration under contract number DE-AC52-06NA25396. M.I., S.-K.L., J.K., C.C., G.L., and Y.Y. acknowledge support from NRFK grant number 2017R1A3A3001362, funded by the Korean government. Work by C.-U.L. and S.-L.K. was supported by the KASI (Korea Astronomy and Space Science Institute) grant 2017-1-830-03. This research made use of the KMTNet system operated by KASI, and the data were obtained at three Cerro-Tololo Inter-American Observatory host sites in Chile, the South African Astronomical Observatory in South Africa, and the Siding Spring Observatory in Australia. E. Troja acknowledges support from grants GO718062A and HSTG014850001A. R.S.-R. acknowledges support by the Italian Space Agency through contract number 2015-046-R.0 and by the European Union Horizon 2020 Programme under the AHEAD project (grant agreement number 654215). T.S. acknowledges support by MEXT KAKENHI (grant numbers 17H06357 and 17H06362).

Author Contributions E. Troja, L.P., H.v.E. and O.K. composed the text, with input from all co-authors. E. Troja and T.S. obtained and analysed the Chandra X-ray observations. Hubble Space Telescope observations were obtained, reduced and analysed by E. Troja, O.D.F., R.E.R. Jr and H.G.K. E. Troja, N.R.B., S.B.C., J.B.G. and R.S.-R. obtained, processed and analysed the Gemini data. M.I., C.-U.L., S.-L.K., J.K., C.C., G. L., H.M.L. led the optical imaging with KMTNet. E. Troja, L.P., R.R. and M.H.W. obtained, processed and analysed the Australia Telescope Compact Array observations. R.T.W., O.K., C.L.F. and C.J.F. led the modelling of the kilonova emission. H.v.E., L.P. and E. Troja led the modelling of the GRB and afterglow emission. A.M.W., W.H.L. and J.M.B. contributed to the spectral modelling. M.I., Y.Y. and S.-K.L. led the analysis of the host galaxy. All authors discussed the results and commented on the manuscript.

Author Information Reprints and permissions information is available at www.nature.com/reprints. The authors declare no competing financial interests. Readers are welcome to comment on the online version of the paper. Publisher's note: Springer Nature remains neutral with regard to jurisdictional claims in published maps and institutional affiliations.
Correspondence and requests for materials should be addressed to E. Troja (eleonora.troja@nasa.gov).

Reviewer Information *Nature* thanks R. Chevalier and C. Miller for their contribution to the peer review of this work.

METHODS

X-ray imaging with the Chandra X-ray Observatory. Chandra observed the counterpart of GW170817 at four different epochs. The first observation, performed at $T_0 + 2.2$ d, did not detect X-ray emission from AT 2017gfo (ref. 31). Our observations (Principal Investigator (PI): E. Troja) were performed at $T_0 + 9$ d and $T_0 + 15$ d for total exposures of 50 ks and 47 ks, respectively. Data were reduced and analysed using standard analysis tools within CIAO v. 4.9 with calibration database CALDB v. 4.7.6. In both epochs we detect X-ray emission at the same position as the optical/infrared transient (see below) at a statistically significant level (false positive probability $P < 10^{-7}$). The source was detected with similarly high significance in a later 47 ks observation at $T_0 + 16$ d (ref. 32).

Photon events from the afterglow were selected using a circular extraction region of radius 1 arcsec, while the background level of 2.3×10^{-6} counts arcsec^{-2} s^{-1} was estimated from nearby source-free regions. In the 0.5–8.0 keV energy band, we measured 12 total counts in our first epoch and 17 total counts in the second epoch. To estimate the source flux, we analysed the spectra[33] within XSPEC v.12.9.1. We used an absorbed power-law model with the absorbing column fixed at the Galactic value $N_{\rm H} = 8.76 \times 10^{20}$ cm^{-2}, and minimized the Cash statistics to find our best fit parameters. The joint fit of the two spectra yielded a photon index $\Gamma = 1.3 \pm 0.4$ and unabsorbed X-ray fluxes of $(4.0 \pm 1.1) \times 10^{-15}$ erg cm^{-2} s^{-1} at $T_0 + 9$ d and $(5.0 \pm 1.0) \times 10^{-15}$ erg cm^{-2} s^{-1} at $T_0 + 15$ d in the 0.3–10 keV energy band. All the quoted errors are at the 68% confidence level. Our results therefore suggest the presence of a slowly rising X-ray emission with $F_{\rm X} \propto t^{0.5}$.

By assuming a similar background level and source spectral shape, we estimate an upper limit to the X-ray flux of 3.7×10^{-15} erg cm^{-2} s^{-1} (95% confidence level) at $T_0 + 2.2$ d, consistent with our findings and the upper limits from Swift and NuSTAR[17].

Hubble Space Telescope observations. We obtained several epochs of imaging and near-infrared grism spectroscopy (PI: E. Troja) with the Hubble Space Telescope[34]. Images were taken with both the infrared and the UVIS detectors of the Wide-Field Camera 3 (WFC3). Data were reduced in a standard fashion using the Hubble Space Telescope CalWF3 standard pipeline[35], and the astrodrizzle processing[36]. Fluxes were converted to magnitudes using WFC3 zero points[37,38]. Our final photometry is shown in Fig. 3b.

We performed relative astrometry between our WFC3/F160W image and our Chandra observations. We identified five common point-like sources (in addition to the gravitational-wave counterpart AT 2017gfo) and excluded those next to the edge of the field of view and with poor signal-to-noise ratio. The remaining three sources were used to register the Chandra image onto the Hubble Space Telescope frame. The corrected X-ray position of AT 2017gfo is offset from the infrared position by $0.14'' \pm 0.22''$ (68% confidence level).

The probability of finding an unrelated X-ray source at such a small offset is $<10^{-5}$ for field objects[39] as well as for an unrelated X-ray binary within the galaxy[40]. Pre-explosion imaging[41] disfavours the presence of a globular cluster at the transient location[42].

Spectroscopic frames were processed with the Hubble Space Telescope CalWF3 standard pipeline. To estimate any possible contribution from the nearby host galaxy, we fitted a second-order polynomial (modelling the galaxy) and a Gaussian (modelling the source) as a function of the y coordinate. We smoothed the resultant contamination model with a Savitzky–Golay filter to remove any high-frequency structure. We then subtracted the background and refitted the remaining source flux with a Gaussian. Finally, we combined the four images (per epoch per grism) using a 3σ-clipped average, rejecting pixels associated with the bad-pixel masks and weighting by the inverse variance. Extended Data Fig. 5 illustrates this process.

Optical and infrared imaging with Gemini-South. We obtained several epochs of optical and infrared imaging (PI: E. Troja) of the gravitational-wave counterpart AT 2017gfo, starting on 21 August 2017. Optical data were acquired with the Gemini Multi-Object Spectrograph (GMOS) mounted on the 8-m Gemini South telescope, and reduced using standard Gemini/Image Reduction and Analysis Facility (IRAF) tasks. We performed point spread function (PSF)-fitting photometry using custom Python scripts after subtracting a Sersic function fit to remove the host galaxy flux. Errors associated with the Sersic fit were measured by smoothing the fit residuals, and then propagated through the PSF fitting. The resulting *griz* photometry, shown in Fig. 3b, was calibrated to Pan-STARRS[43] using a common set of field stars for all frames. Infrared images (JHKs bands) were acquired with the Flamingos-2 instrument. Data were flat-fielded and sky-subtracted using custom scripts designed for the RATIR project (http://www.ratir.org). Reduced images were aligned and stacked using SWarp (http://astromatic.net/software/swarp). The PSF photometry was calculated, after host galaxy subtraction, and calibrated to a common set of 2MASS[44] sources, using the 2MASS zero points to convert to the AB system.

Optical imaging with KMTNet. Three Korea Microlensing Telescope Network (KMTNet) 1.6-m telescopes[45] observed the counterpart of GW170817 nearly every night starting on 18 August 2017 at three locations, the South African Astronomical Observatory in South Africa, the Siding Spring Observatory in Australia, and the Cerro-Tololo Inter-American Observatory in Chile. The observations were made using the B, V, R and I filters. Data were reduced in a standard fashion. Reference images taken after 31 August were used to subtract the host galaxy contribution. Photometry was performed using SExtractor, and calibrated using the AAVSO Photometric All-Sky Survey (APASS) catalogue. Our final photometry is shown in Fig. 3b. We also include publicly released data from refs 46–50.

Optical spectroscopy with Gemini. We obtained optical spectroscopy (PI: E. Troja) of the gravitational-wave counterpart AT 2017gfo with GMOS beginning at 23:38 UT on 20 August 2017. A series of four spectra, each 360 s in duration, were obtained with both the R400 and B600 gratings (see also ref. 49). We employed the 1.0″ slit for all observations. All data were reduced with the Gemini IRAF (v. 1.14) package following standard procedures. The resulting spectrum of AT 2017gfo is plotted in Fig. 2. The spectrum exhibits a relatively red continuum, with a turnover around 7,500 Å. The lack of strong absorption features is consistent with the low estimated extinction along the sightline[51], $E_{\rm B-V} = 0.105$, and suggests that there is no substantial intrinsic absorption. No narrow or broad features, such as those that are typically observed in all types of core-collapse supernova, are apparent.

We attempted to spectroscopically classify the source using the SuperNova IDentification (SNID) code[52], with the updated templates for stripped-envelope supernovae. No particularly good match was found, even using this expanded template set. In this case SNID often defaults to classifications of type Ib/c (typically of the broad-lined sub-class), owing to the broad (and therefore typically weaker) nature of the features. For comparison in Fig. 2 we plot the spectrum of the prototypical broad-lined type Ic supernova SN 1998bw[53]. It is evident the source is not a good match. Even after removing the continuum ('flattening'), the match to mean spectral templates of broad-lined type Ic supernovae[54] is quite poor.

Radio observations with the Australia Telescope Compact Array. We observed the target with the Australia Telescope Compact Array at three different epochs ($T_0 + 14.5$ d, $T_0 + 20.5$ d and $T_0 + 28.5$ d) at the centre frequencies 16.7 GHz, 21.2 GHz, 43 GHz and 45 GHz in continuum mode (PI: E. Troja). The data were reduced with the data reduction package MIRIAD[55] using standard procedures. Radio images were formed at 19 GHz and 44 GHz via the Multi Frequency Synthesis technique. No detection was found at the position of the optical/infrared transient; our upper limits are shown in Fig. 3a. During the time interval covered by our observations, detections of the radio afterglow at 3 GHz and 6 GHz were reported[18,49] at a level of about 35 μJy.

Properties of the host galaxy NGC 4993. In terms of morphology, NGC 4993 shows an extended, disturbed feature and prominent dust lanes in the inner region (Fig. 1a), suggestive of a minor merger in the past. From the Ks-band images we derive an absolute magnitude of $M_{\rm K} \approx -22$ AB mag and a stellar mass of $\log(M/M_{\odot}) \approx 10.9$, calculated by assuming a stellar-mass-to-light ratio of the order of unity[56]. Structural parameters were derived from our F110W and F160W image using GALFIT. A fit with a single Sersic component yields an index of 5.5, an ellipticity of about 0.12, and an effective radius $R_{\rm e} \approx 3.4$ kpc. The lack of emission lines in our spectra suggests little to no ongoing star formation at the location of the neutron-star merger, consistent with the low ultraviolet luminosity $M_{\rm F275W} > -7.5$ AB mag (95% confidence level) in the vicinity of the transient. Indeed, the measured Lick indices[57] with $\rm H\beta = 1.23$ and $\rm [MgFe] = 3.16$ and the modelling of the spectral energy distribution suggest an old (>2 billion years), evolved stellar population of solar or slightly sub-solar metallicity (Extended Data Fig. 6). The overall properties of NGC 4993 are therefore consistent with an early-type galaxy, and within the range of galaxies harbouring short GRBs[5].

In the nuclear region of NGC 4993, our radio observations show a persistent and relatively bright radio source with flux 420 ± 30 μJy at 19 GHz. The same source is not visible at 44 GHz, indicating a steep radio spectrum. The central radio emission suggests the presence of a low-luminosity active galactic nucleus contributing to the X-ray emission from the galaxy centre (Fig. 1b). Active galactic nucleus activity in a GRB host galaxy is rarely observed, but is not unprecedented[58] in nearby short GRBs.

Off-axis GRB modelling. We interpret the radio and X-ray emission as synchrotron radiation from a population of shock-accelerated electrons. By assuming that radio and X-rays belong to the same synchrotron regime, we derive a spectral slope of 0.64, consistent with the value measured from the X-ray spectrum $\beta = \Gamma - 1 = 0.3 \pm 0.4$. This corresponds to the spectral regime between the injection frequency $\nu_{\rm m}$ and the cooling frequency $\nu_{\rm c}$ for a non-thermal electron population with power-law index 2.3, close to its typical value of GRB afterglows[59]. The presence of a cooling break between radio and X-rays would imply a lower value for the power-law index. The apparent flattening of the X-ray light curve, and the fact

that the two observations adjacent to the radio detection are upper limits, suggest that the detections were close to a temporal peak of the light curve.

We assume that the radio and X-ray detections correspond to afterglow emission from a GRB jet observed at an angle, with the observer placed at an angle θ_v outside the initial jet opening angle θ_j (Fig. 4). We test two implementations of this assumption for consistency with the data, a semi-analytic simplified spreading homogeneous shell model[11] and light curves derived from a series of high-resolution two-dimensional relativistic hydrodynamics simulations[27].

Standard afterglow models[60] contain at least six free variables: θ_j, θ_v, the isotropic equivalent jet energy E_{iso}, ambient medium number density n_0, the magnetic field energy fraction ε_B and the accelerated electron energy fraction ε_e. These are too many parameters to be constrained by the observations. We therefore take 'standard' values for model parameters ($\varepsilon_B \approx 0.01$, $\varepsilon_e \approx 0.1$, $n_0 \approx 10^{-3}$, $\theta_j \approx 15°$), and choose E_{iso} and θ_v to match the observations. We caution that the displayed match demonstrates only one option in a parameter space that is degenerate for the current number of observational constraints. A key feature of interest is the peak time, which is plausibly constrained by the current observations. This scales according to $t_{peak} \propto (E_{iso}/n_0)^{1/3}\Delta\theta^{2.5}$, which follows from complete scale-invariance between curves of different energy and density[61], and from a survey of off-axis curves for different $\Delta\theta$ using the semi-analytical model. Note that the scaling applies to the temporal peak, and not to the moment t_{start} when the off-axis signal starts to become visible, where $t_{start} \propto \Delta\theta^{8/3}$ (similar to a jet break). The scaling of 2.5 is slightly shallower and reflects the trans-relativistic transition as well. From our model comparisons to data, we infer an offset of $\Delta\theta \approx 13°$.

If a dense wind exists directly surrounding the jet, a cocoon of shocked dense material and slower jet material has been argued to exist and emerge with the jet in the form of a slower-moving outflow[62,63]. When emitted quasi-isotropically, or seen on-axis, cocoon afterglows are, however, expected to peak at far earlier times (hours after T_0) than currently observed[64,65]. A more complex initial shape of the outflow than a top hat, such as a structured jet[66] with a narrow core and an angle for the wings that is smaller than the observer angle, will have one additional degree of freedom. It is not possible to distinguish between the fine details of the various models: at the time of the observations, top-hat jets, structured jets and collimated cocoon-type outflows are all decelerating and spreading blast waves segueing from relativistic origins into a non-relativistic stage, and all are capable of producing a synchrotron afterglow through a comparable mechanism. At this stage we cannot rule out a broad flat X-ray/radio peak or additional brightening due to jet structure, nor a subsequent emergent contribution from kilonova ejecta interaction with the ambient medium.

Origin of the γ-ray emission. For a standard top-hat GRB jet[67], the peak energy E_{peak} and the total energy release E_{iso} scale as a and a^{-3}, where $a^{-1} \approx 1 + \Gamma^2\Delta\theta^2$ and $\Delta\theta > 1/\Gamma$. By assuming typical values of $E_{iso} \approx 2 \times 10^{51}$ erg, $E_{peak} \approx 1$ MeV, and a Lorentz factor of $\Gamma \approx 100$ to avoid opacity due to pair production and Thomson scattering[26], the expected off-axis γ-ray emission would be much fainter than GRB 170817A. This suggests that the observed γ-rays might come from a different and probably isotropic emission component, such as precursors[68] seen in some short GRBs or a mildly relativistic cocoon[64].

A different configuration is the one of a structured jet, where the energetics and Lorentz factor of the relativistic flow depend upon the viewing angle[66,69]. In this case, the observed flux is dominated by the elements of the flow pointing close to the line of sight. For a universal jet, a power-law dependence is assumed with $E_{\gamma,iso}(\theta_v) \propto (\theta_v/\theta_c)^{-2}$, where θ_c is the core of the jet. For a Gaussian jet, the energy scales as $E_{\gamma,iso}(\theta_v) \propto \exp(-\theta_v^2/2\theta_c^2)$. Owing to its substantial emission at wide angles, a universal jet fails to reproduce the afterglow data (Extended Data Fig. 3). A Gaussian jet with standard isotropic energy $E_{\gamma,iso} \approx 2 \times 10^{51}$ erg can instead reproduce the observed energetics[13,14] of GRB 170817A ($E_{\gamma,iso} \approx 5 \times 10^{46}$ erg when $\theta_v \approx 4\theta_c$. The same jet can also describe the broadband afterglow data (Extended Data Fig. 3), thus representing a consistent model for the prompt and afterglow emissions.

Kilonova modelling. Our kilonova (or macronova) calculations are based on the approach developed by ref. 30. We use the multigroup, multidimensional radiative Monte Carlo code SuperNu[70–72] (https://bitbucket.org/drrossum/supernu/wiki/Home) with the set of opacities produced by the Los Alamos suite of atomic physics codes[73–75]. For this paper, we build upon the range of two-dimensional simulations[30] using the class A ejecta morphologies and varying the ejecta mass, velocity, composition and orientation as well as the model for energy deposition in post-nucleosynthetic radioactive decays. Our nuclear energy deposition is based on the finite-range droplet model (FRDM) of nuclear masses.

Kilonova light-curves can be roughly separated into two components: an early peak dominated by the wind ejecta (where by 'wind' we indicate the entire variety of secondary post-merger outflows, with many elements in the atomic mass range between the iron peak up through the second r-process peak) and a late infrared peak that is powered by the lanthanide-rich (main r-process elements) dynamical ejecta. The luminous optical and ultraviolet emission[17] require a large wind mass ($M_w > (0.015–0.03)M_\odot$) and a composition with moderate neutron richness ('wind 2' with $Y_e = 0.27$ from ref. 30). A large fraction of these ejecta consists of first peak r-process elements. The late-time infrared data probe the properties of the dynamical ejecta ($Y_e < 0.2$), arguing for a mass of $M_{ej} \approx (0.001–0.01)M_\odot$. This ejecta is primarily composed of the main r-process elements lying between the second and third r-process peaks (inclusive). Within the errors of our modelling, the low inferred ejecta mass combined with the high rate of neutron-star mergers inferred from this gravitational-wave detection is in agreement with the neutron-star merger being the main site of the r-process production[76]. However, our models seem to overproduce the first peak r-process relative to the second and third peaks. This could be due to the model simplifications in the treatment of ejecta composition, or it could be because this particular event is not standard for neutron-star mergers.

Another, more plausible, source of error comes from the uncertainties in nuclear physics, such as the nuclear mass model used in the r-process nucleosynthesis calculation. Our baseline nuclear mass model (FRDM[77]) tends to underestimate the nuclear heating rates, compared to other models such as the DZ31 model[78]. Specifically, in the latter model the abundances of trans-lead elements can dramatically alter the heating at late times[76,79]. Combined differences in the heating rate and thermalization translate to nearly a factor of 10 in the nuclear energy deposition at late times[79] ($t > 2$ days). We have therefore adjusted the heating rate in the dynamical ejecta to compensate for this effect. If this nuclear heating rate is too high, then we are underestimating the mass of the dynamical ejecta.

The opacity of the lanthanide-rich tidal ejecta is dominated by a forest of lines up to the near-infrared, causing most of the energy to escape beyond 1 μm, and one indicator of ejecta dictated by lanthanide opacities is a spectrum peak above 1 μm that remains relatively flat in the infrared. However, standard parameters for the ejecta predict a peak between 5 and 10 days. To fit the early peak (about 3 days) requires either a lower mass, or higher velocities. Our best-fit model has a tidal/dynamic ejecta mass of $M_{ej} \approx 0.002M_\odot$ and median velocity (approximately $v_{peak}/2$) of $0.2c$.

Extended Data Fig. 4 shows our synthetic light curves for different viewing angles. In the on-axis orientation, the observer can see both types of outflows, while in the edge-on orientation the wind outflow is completely obscured. The system orientation most strongly affects the behaviour in the blue optical bands, while the infrared bands are largely unaffected. The observed slow decline in the optical bands for this event is best fitted by moderate-latitude viewing angles (about 20°–60°).

Data availability. All relevant data are available from the corresponding author on reasonable request. Data presented in Fig. 3b are included as Source Data with the online version of the paper.

31. Margutti, R. *et al.* The electromagnetic counterpart of the binary neutron star merger LIGO/VIRGO GW170817. V. Rising X-ray emission from an off-axis jet. *Astrophys. J.* **848,** http://doi.org/10.3847/2041-8213/aa9057 (2017).
32. Haggard, D. *et al.* A deep Chandra X-Ray study of neutron star coalescence GW170817. *Astrophys. J.* **848,** http://doi.org/10.3847/2041-8213/aa8ede (2017).
33. Arnaud, K. A. XSPEC: the first ten years. *Astron. Data Analysis Softw. Syst. V* **101,** 17–20 (1996).
34. Tanvir, N. R. *et al.* The emergence of a lanthanide-rich kilonova following the merger of two neutron stars. *Astrophys. J.* (https://doi.org/10.3847/2041-8213/aa90b6). (2017).
35. Deustua, S. (ed.) *WFC3 Data Handbook* Version 3.0, http://www.stsci.edu/hst/wfc3/documents/handbooks/currentDHB/wfc3_cover.html (Space Telescope Science Institute (STScI), 2016).
36. Gonzaga, S., Hack, W., Fruchter, A. & Mack, J. (eds) *The DrizzlePac Handbook* http://www.stsci.edu/hst/HST_overview/drizzlepac/documents/handbooks/drizzlepac.pdf (Space Telescope Science Institute (STScI), 2012).
37. Deustua, S. E., Mack, J., Bajaj, V. & Khandrika, H. WFC3/UVIS Updated 2017 Chip-Dependent Inverse Sensitivity Values. Instrument Science Report WFC3, 14, http://www.stsci.edu/hst/wfc3/documents/ISRs/WFC3-2017-14.pdf (Space Telescope Science Institute (STScI), 2017).
38. Deustua, S. E., Mack, J., Bajaj, V. & Khandrika, H. Hubble Space Telescope IR photometric calibration. http://www.stsci.edu/hst/wfc3/analysis/ir_phot_zpt (Space Telescope Science Institute (STScI), 2017).
39. Mateos, S. *et al.* High precision X-ray log N–log S distributions: implications for the obscured AGN population. *Astron. Astrophys.* **492,** 51–69 (2008).
40. Swartz, D. A., Soria, R., Tennant, A. F. & Yukita, M. A complete sample of ultraluminous X-ray source host galaxies. *Astrophys. J.* **741,** 49 (2011).
41. Bellini, A., Grogin, N. A., Hathi, N. & Brown, T. M. The Hubble Space Telescope "Program of Last Resort". Instrument Science Report ACS/WFC 2017-12, http://www.stsci.edu/hst/acs/documents/isrs/isr1712.pdf (Space Telescope Science Institute (STScI), 2017).
42. Levan, A. J. *et al.* The environment of the binary neutron star merger GW170817. *Astrophys. J.* **848,** http://doi.org/10.3847/2041-8213/aa905f (2017).

43. Chambers, K. C. *et al.* The Pan-STARRS1 surveys. Preprint available at https://arxiv.org/abs/1612.05560 (2016).
44. Skrutskie, M. F. *et al.* The Two Micron All Sky Survey (2MASS). *Astron. J.* **131,** 1163–1183 (2006).
45. Kim, S.-L. *et al.* KMTNET: a network of 1.6 m wide-field optical telescopes installed at three southern observatories. *J. Korean Astron. Soc.* **49,** 37–44 (2016).
46. Smartt, S. J. *et al.* A kilonova as the electromagnetic counterpart to a gravitational-wave source. *Nature* http://doi.org/10.1038/nature24303 (2017).
47. Pian, E. *et al.* Spectroscopic identification of r-process nucleosynthesis in a double neutron-star merger. *Nature* http://doi.org/10.1038/nature24298 (2017).
48. Drout, M. R. *et al.* Ultraviolet to near-infrared light curves of GW170817/SSS17a - implications for the r-process. *Science* http://doi.org/10.1126/science.aaq0049 (2017).
49. Kasliwal, M. M. *et al.* Illuminating gravitational waves: a concordant picture of photons from a neutron star merger. *Science* http://doi.org/10.1126/science.aap9455 (2017).
50. Chornock, R. *et al.* The electromagnetic counterpart of the binary neutron star merger LIGO/VIRGO GW170817. IV. Detection of near-infrared signatures of r-process nucleosynthesis with Gemini-South. *Astrophys. J.* **848,** https://doi.org/10.3847/2041-8213/aa905c (2017).
51. Schlafly, E. F. & Finkbeiner, D. P. Measuring reddening with Sloan Digital Sky Survey stellar spectra and recalibrating SFD. *Astrophys. J.* **737,** 103 (2011).
52. Blondin, S. & Tonry, J. Determining the type, redshift, and age of a supernova spectrum. *Astrophys. J.* **666,** 1024–1047 (2007).
53. Patat, F. *et al.* The metamorphosis of SN 1998bw. *Astrophys. J.* **555,** 900–917 (2001).
54. Modjaz, M., Liu, Y. Q., Bianco, F. B. & Graur, O. The spectral SN-GRB connection: systematic spectral comparisons between type Ic supernovae and broad-lined type Ic supernovae with and without gamma-ray bursts. *Astrophys. J.* **832,** 108–131 (2016).
55. Sault, R. J., Teuben, P. J. & Wright, M. C. H. A retrospective view of MIRIAD. *Astron. Data Anal. Softw. Syst. IV* **77,** 433 (1995).
56. Kim, D. & Im, M. Optical-near-infrared color gradients and merging history of elliptical galaxies. *Astrophys. J.* **766,** 109–135 (2013).
57. Ogando, R. L. C., Maia, M. A. G., Pellegrini, P. S. & Da Costa, L. N. Line strengths of early-type galaxies. *Astron. J.* **135,** 2424–2445 (2008).
58. Xie, C., Fang, T., Wang, J., Liu, T. & Jiang, X. On the host galaxy of GRB 150101B and the associated active galactic nucleus. *Astrophys. J.* **824,** L17 (2016).
59. Ryan, G., van Eerten, H., MacFadyen, A. & Zhang, B.-B. Gamma-ray bursts are observed off-axis. *Astrophys. J.* **799,** 3 (2015).
60. Sari, R., Piran, T. & Narayan, R. Spectra and light curves of gamma-ray burst afterglows. *Astrophys. J.* **497,** L17–L20 (1998).
61. van Eerten, H. J. & MacFadyen, A. I. Gamma-ray burst afterglow scaling relations for the full blast wave evolution. *Astrophys. J.* **747,** L30 (2012).
62. Nagakura, H., Hotokezaka, K., Sekiguchi, Y., Shibata, M. & Ioka, K. Jet collimation in the ejecta of double neutron star mergers: a new canonical picture of short gamma-ray bursts. *Astrophys. J.* **784,** L28 (2014).
63. Morsony, B. J., Workman, J. C. & Ryan, D. M. Modeling the afterglow of the possible Fermi-GBM event associated with GW150914. *Astrophys. J.* **825,** L24 (2016).
64. Lazzati, D., Deich, A., Morsony, B. J. & Workman, J. C. Off-axis emission of short γ-ray bursts and the detectability of electromagnetic counterparts of gravitational-wave-detected binary mergers. *Mon. Not. R. Astron. Soc.* **471,** 1652–1661 (2017).
65. Gottlieb, O., Nakar, E. & Piran, T. The cocoon emission—an electromagnetic counterpart to gravitational waves from neutron star mergers. Preprint at https://arxiv.org/abs/1705.10797 (2017).
66. Rossi, E., Lazzati, D. & Rees, M. Afterglow light curves, viewing angle and the jet structure of γ-ray bursts. *Mon. Not. R. Astron. Soc.* **332,** 945–950 (2002).
67. Granot, J., Panaitescu, A., Kumar, P. & Woosley, S. E. Off-axis afterglow emission from jetted gamma-ray bursts. *Astrophys. J.* **570,** L61–L64 (2002).
68. Troja, E., Rosswog, S. & Gehrels, N. Precursors of short gamma-ray bursts. *Astrophys. J.* **723,** 1711–1717 (2010).
69. D'Alessio, V., Piro, L. & Rossi, E. M. Properties of X-ray rich gamma ray bursts and X-ray flashes detected with BeppoSAX and Hete-2. *Astron. Astrophys.* **460,** 653–664 (2006).
70. Wollaeger, R. T. *et al.* Radiation transport for explosive outflows: a multigroup hybrid Monte Carlo method. *Astrophys. J. Suppl. Ser.* **209,** 36 (2013).
71. Wollaeger, R. T. & van Rossum, D. R. Radiation transport for explosive outflows: opacity regrouping. *Astrophys. J. Suppl. Ser.* **214,** 28 (2014).
72. van Rossum, D. R. *et al.* Light curves and spectra from a thermonuclear explosion of a white dwarf merger. *Astrophys. J.* **827,** 128 (2016).
73. Fontes, C. J. *et al.* Relativistic opacities for astrophysical applications. *High Energy Density Phys.* **16,** 53–59 (2015).
74. Fontes, C. J. *et al.* A line-smeared treatment of opacities for the spectra and light curves from macronovae. Preprint at https://arxiv.org/abs/1702.02990 (2017)
75. Fontes, C. J. *et al.* The Los Alamos suite of relativistic atomic physics codes. *J. Phys. At. Mol. Opt. Phys.* **48,** 144014 (2015).
76. Rosswog, S. *et al.* Detectability of compact binary merger macronovae. *Class. Quantum Gravity* **34,** 104001 (2017).
77. Duflo, J. & Zuker, A. P. Microscopic mass formulas. *Phys. Rev. C* **52,** 23–27 (1995).
78. Barnes, J., Kasen, D., Wu, M.-R. & Martine-Pinedo, G. Radioactivity and thermalization in the ejecta of compact object mergers and their impact on kilonova light curves. *Astrophys. J.* **829,** 110 (2016).
79. Moller, P., Nix, J. R., Myers, W. D. & Swiatecki, W. J. Nuclear ground-state masses and deformations. *At. Data Nucl. Data Tables* **59,** 185 (1995).
80. Bruzual, G. & Charlot, S. Stellar population synthesis at the resolution of 2003. *Mon. Not. R. Astron. Soc.* **344,** 1000–1028 (2003).
81. Chabrier, G. Galactic stellar and substellar initial mass function. *Publ. Astron. Soc. Pacif.* **115,** 763–795 (2003).

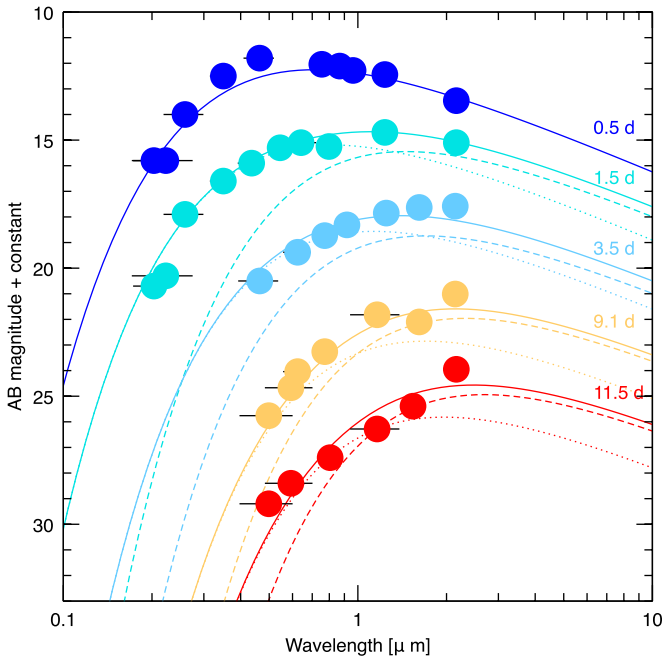

Extended Data Figure 1 | Spectral energy distributions of the optical/infrared counterpart. We can empirically describe the spectral energy distribution and its temporal evolution as the superposition of two blackbody components in linear expansion. A single component provides a good fit at early times ($T_0 + 0.5$ d), but at later times we find that two components (shown by the dashed and dotted lines) with different temperatures and expansion velocities represent a better description of the dataset. The large effective radii ($R > 4 \times 10^{14}$ cm at $T_0 + 0.5$ d) inferred from the blackbody fits imply an average velocity $v > 0.2c$. Magnitudes are corrected for Galactic extinction along the line of sight[51]. Data have been shifted for plotting purposes.

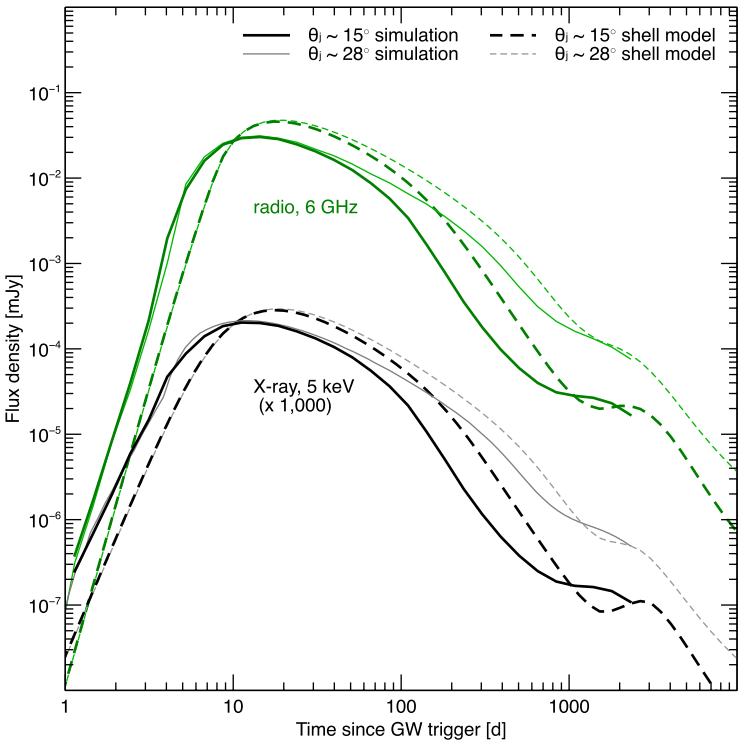

Extended Data Figure 2 | Models of off-axis afterglows at X-ray and radio energies. Direct comparison between off-axis light curves for two different jet opening angles θ_j (15° and 28°). As long as the difference between the viewing angle and the jet angle is maintained, a continuous range of jet angles can be found that is consistent with the observations in X-rays and at radio wavelengths, mostly covering the peak. Dashed lines show light curves computed using the semi-analytic spreading top-hat jet model[11] for identical input parameters. Note that the simulated angular fluid profile quickly becomes complex as the jet evolves, and the similarity in light curves to those derived from the top-hat shell illustrate that the global features do not depend strongly on this angular profile. The simulated light curves include synchrotron self-absorption, which was not found to be important for the current parameters. (GW, gravitational wave.)

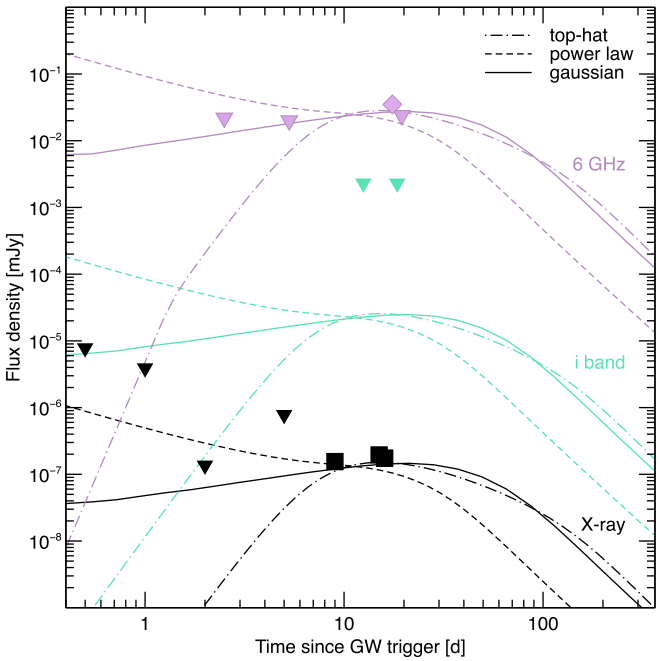

Extended Data Figure 3 | Afterglow modelling for different jet profiles viewed at an angle. We consider three well known jet profiles: top-hat (dot-dashed line), Gaussian (solid line), and power law (dashed line). A power-law structured jet is not consistent with the lack of afterglow detection at early times. A top-hat jet and a Gaussian structured jet can both describe the afterglow behaviour, and imply a large off-axis angle. The Gaussian jet has the additional advantage of consistently explaining both the prompt γ-rays and the afterglow emission.

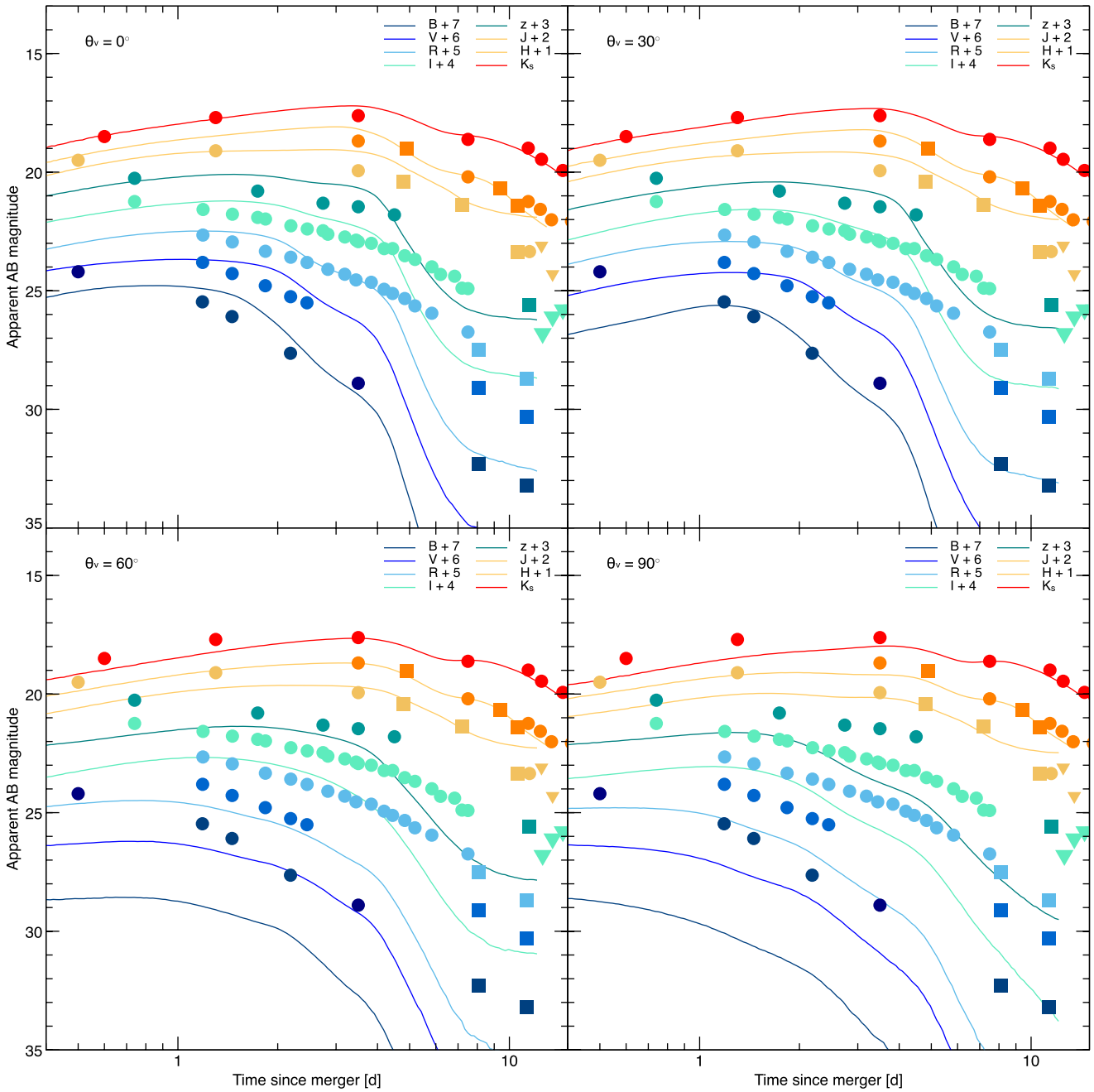

Extended Data Figure 4 | Kilonova light curves as a function of the viewing angle. Comparison of the observational data with the synthetic light curves from the two-component axisymmetric radiative transfer model at different viewing angles: 0° (on-axis view); 30°, 60° and 90° (edge-on equatorial view). Our model includes a wind with mass $M_w \approx 0.015 M_\odot$ and velocity $v_w \approx 0.08c$, and dynamical ejecta with mass $M_{ej} \approx 0.002 M_\odot$ and velocity $v_{ej} \approx 0.2c$.

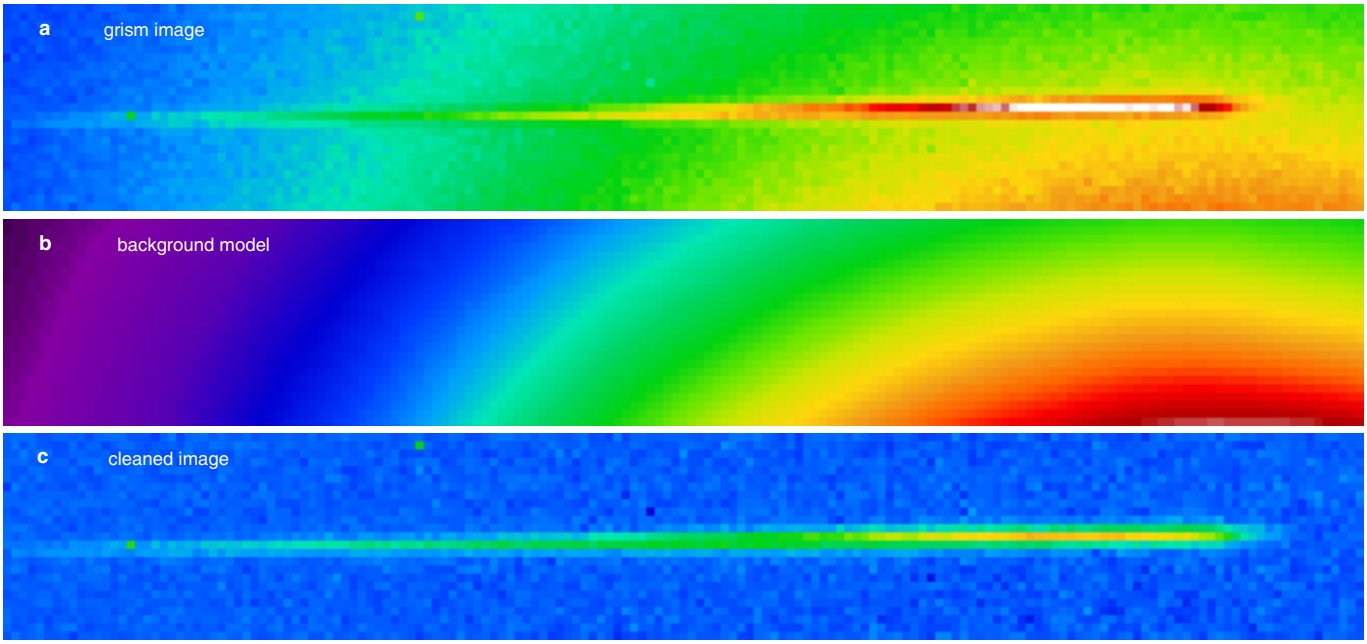

Extended Data Figure 5 | Illustrative example of the contamination modelling. a, Two-dimensional dispersed image at the position of AT 2017gfo. **b**, Our model describing the emission from NGC 4993, smoothed with a Savitzky–Golay filter in order to remove any high-frequency structure. **c**, Difference between the data and the model.

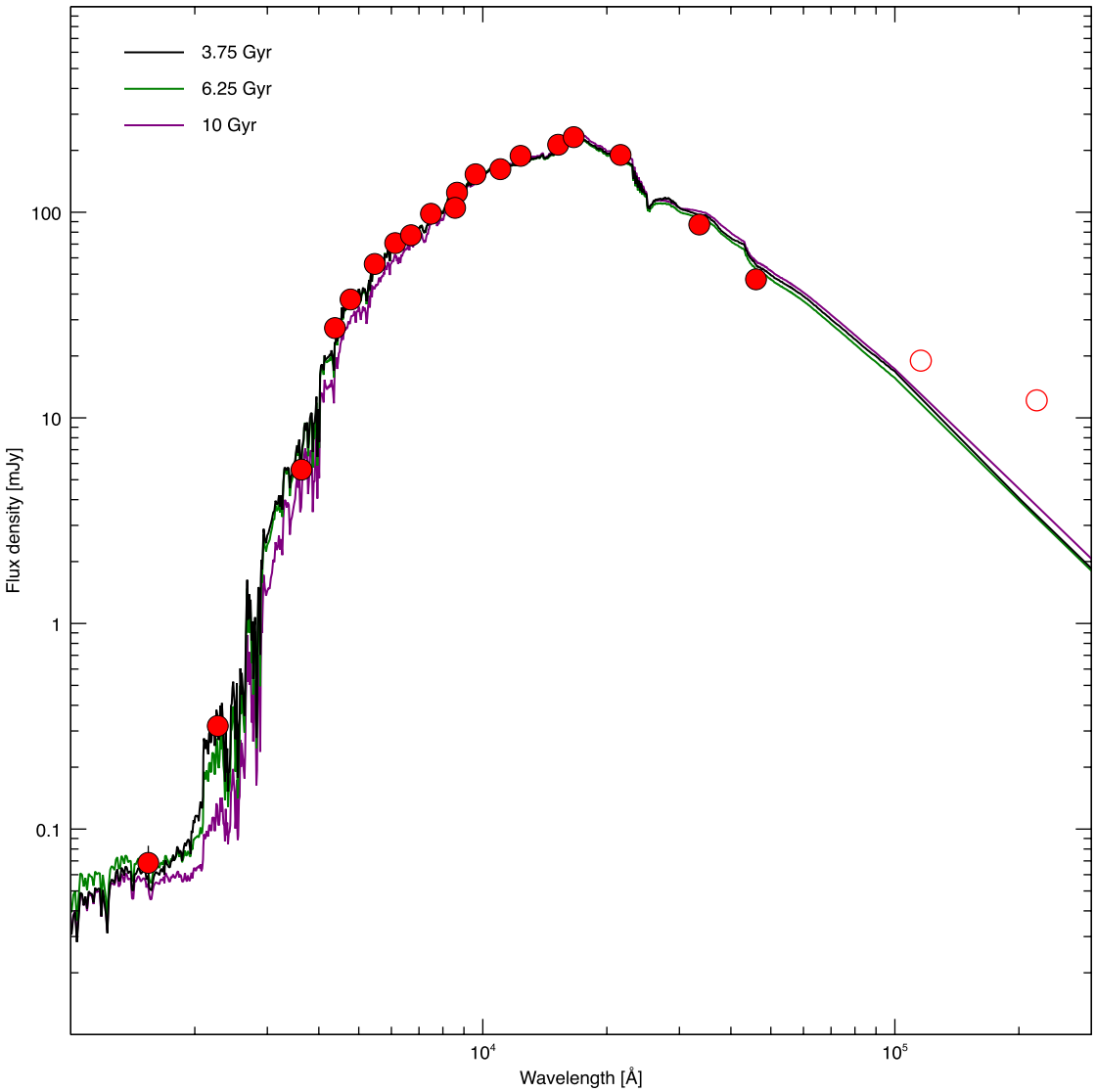

Extended Data Figure 6 | Broadband spectral energy distribution of NGC 4993. The model assumes a delayed star-formation rate, standard spectral templates[80] and initial mass function[81]. Models for three different stellar ages are shown. Fluxes are corrected for Galactic extinction along the line of sight[51]. Vertical error bars are 1σ. Data above 5,000 Å (open circles) are not used in the fit as they may be affected by emission from dust. The modelling of the spectral energy distribution favours a mean stellar age of 3–7 billion years (Gyr) and disfavours ages less than 2 Gyr. The mean stellar mass is found to be in the range of $(5–10) \times 10^{10} M_{\odot}$ with a solar metallicity.